Analogue experiments on the rise of large bubbles through a solids-rich suspension: a "weak plug" model for Strombolian eruptions

Oppenheimer J.[1*], Capponi A.[2], Cashman K. V.[3], Lane S. J.[2], Rust A. C.[3], James M. R.[2]

1. Lamont-Doherty Earth Observatory with Columbia University, New York, USA; 2. Lancaster Environment Centre, Lancaster University, Lancaster, UK; 3. Department of Earth Sciences, University of Bristol, Bristol, UK.

* Corresponding author: Julie Oppenheimer. Email address: jo0231@my.bristol.ac.uk
Lamont-Doherty Earth Observatory with Columbia University,
61 route 9W – PO Box 1000, Palisades, NY 10964, USA

Abstract

Physical interactions between bubbles and crystals affect gas migration and may play a major role in eruption dynamics of crystal-rich magmas. Strombolian eruptions represent an end member for bubble-crystal interactions, in which large bubbles (significantly larger than the crystal size) rise through a crystal-rich near-surface magma. Indeed, volcanoes that produce Strombolian eruptions often generate ejecta with > 30 vol% (often > 45 vol%) average crystallinity. At Stromboli Volcano, Italy, average crystallinity can reach 55 vol%, which is approaching the eruptibility limit for magmas. At such high crystallinities the solids interact mechanically with each other and with bubbles. This complex rheology complicates the two-phase (liquid-gas) slug flow model often applied to Strombolian eruptions. To examine the effect of crystals on bubble rise, we performed analogue experiments in which large bubbles rise in a vertical tube filled with silicone oil and polypropylene particles. The particles have a slightly lower density than the oil, and therefore form a layer of oil + particles at the upper surface. We varied surface pressure, particle volume fraction, length of the particle-bearing cap, and bubble size to examine the ways in which these parameters influence Strombolian-type eruptions. We show that in experiments, suspended solids begin to affect bubble rise dynamics at particle volume fractions as low as 30 vol% (or, when divided by the random close packing value, a normalized particle fraction φ = 0.64). Bubbles in experiments with higher particle contents deform as they rise and burst through a small aperture, generating surface fountains that begin abruptly and decay slowly, and longer-lasting acoustic signals of lower amplitude than in crystal-poor experiments. In the experiments, particle fractions > 37 vol% (φ > 0.80) generated strong deformations on fast-expanding bubbles that applied a high stress on the cap, but they trapped bubbles that were less overpressured. Qualitatively, the gas release behavior observed in particle-rich experiments is consistent with observations of Strombolian eruptions. Moreover, we estimate that the observed crystallinity of pyroclasts at Stromboli volcano represents $\varphi > 0.8$. From this we suggest a "weak plug" model for Strombolian eruptions that evolves towards a low-viscosity

equivalent of Vulcanian-style plug failure with a more crystalline, stronger, and less permeable plug. Importantly, this model allows the rise of several bubbles in the conduit at the same time and suggests that longer-lasting, more pulsatory and complex eruptions may reveal an increase in near-surface crystallinity, shedding some light on changing conduit conditions that could help determine the different gas rise regimes involved in passive degassing, puffing, and different expressions of Strombolian explosions.

Keywords: Eruption dynamics; Stromboli; Source mechanism; three-phase magma; Conduit processes; Analogue experiments

1. Introduction

Strombolian eruptions are generally small and frequent, but can be associated with dangerous paroxysms, as demonstrated by recent explosions at Stromboli volcano, Italy (2019), and Fuego, Guatemala (2018). In this way, Strombolian eruptions provide direct (and often long-term) insight into changes in conduit conditions that precede and follow hazardous activity. Nevertheless, while Strombolian eruptions are intensively studied (primarily at Stromboli volcano), our interpretation of their source dynamics is hindered by a major flaw: the traditional two-phase model for Strombolian eruptions neglects the effect of crystals on bubble rise, despite the crystal-rich nature of pyroclasts associated with this activity.

Most models for Strombolian eruptions consider Taylor bubbles (slugs) ascending in a Newtonian liquid (e.g. Seyfried and Freundt, 2000; Blackburn et al., 1976; Vergniolle, 1998; Del Bello et al., 2012; Hasan et al., 2019). As slugs expand during ascent, their internal pressure exceeds that in the magma column above; this self-sustained bubble expansion accelerates the overlying liquid to accommodate the gas volume change and increases bubble overpressure at burst (James et al., 2008, 2009; Del Bello et al., 2012; Lane et al., 2013).

However, pyroclasts ejected by many Strombolian eruptions have moderate to high crystallinities. For example, pyroclasts contain >55 vol% crystals at Etna, Italy (Polacci et al., 2006; Giordano et al., 2010; Edwards et al., 2018); 30-40 vol% at Yasur, Vanuatu (Metrich et al., 2011); 45 – 55 vol% at

Stromboli, Italy (Metrich et al., 2010; Landi et al. 2011). This evidence has motivated models involving more complex near-surface processes including magma mingling (Lautze and Houghton, 2005), conduit convection (Landi et al., 2004, 2011; Beckett et al., 2014), and near-surface rheological changes (e.g. Gurioli et al., 2014; Del Bello et al., 2015; Gaudin et al., 2017).

Scaled analogue experiments with gas slugs ascending from a low to high viscosity Newtonian liquid have explored the effects of a near-surface viscous transition on slug flow in a cylindrical conduit (Del Bello et al., 2015; Capponi et al., 2016, 2017). These investigations proposed three geometrical configurations of the slug-cap interactions based on the viscosity of the upper layer (the viscous "cap") and the size of the cap relative to the bubble volume (Figure 1). Longer and more viscous caps impede bubble expansion (hence compress bubbles) below the cap, which affects pressure signals recorded at the base of the experiment, burst processes, and acoustic signals at the surface.

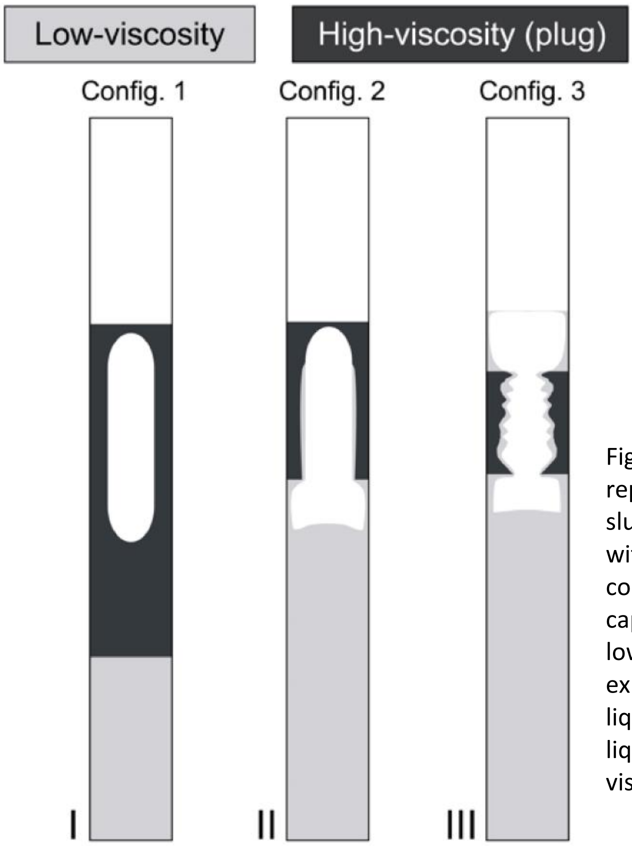

Figure 1: Flow configurations in Capponi et al. (2016, reprinted with permission). In configuration 1 (I), the slug is small enough to be fully accommodated within the cap and bursts at the cap surface. In configuration 2 (II), the bubble nose bursts from the cap into the air above while its tail is still in the lower liquid. In configuration 3 (III), bubble expansion during rise causes the lower viscosity liquid to intrude through the upper more viscous liquid, such that bubble burst occurs in the low-viscosity liquid that is emplaced above the cap.

High magma crystallinity will not only increase viscosity but also create a non-Newtonian rheology. Rheometry of synthetic and analogue magmas demonstrates that high crystallinities (> ~20-40 vol% in basalts) produce both yield strengths and shear-thinning behavior (e.g. Hoover et al., 2001; Jerram et al., 2003; Caricchi et al., 2007; Mueller et al., 2010; Picard et al., 2013; Moitra and Gonnermann, 2015). Consequently, the slug model has been modified to include both shear-thinning rheology and an increasing viscosity towards the surface, which affect bubble overpressures at burst (Von der Lieth and Hort, 2016). In contrast, Suckale et al. (2016) depart from the slug model, suggesting that Strombolian eruptions occur by tensile failure of a porous, rigid plug, generated by bubble overpressure below the plug and aided by regional tectonic stress.

Solid particles also directly affect bubbles by trapping, deforming, and/or splitting them (Belien et al., 2010; Tran et al., 2015; Oppenheimer et al., 2015; Lindoo et al., 2017; Barth et al., 2019). Migration regimes of growing bubbles depend primarily on particle concentrations (Oppenheimer et al., 2015). At low particle fractions, the liquid-particle suspension is approximately Newtonian and growing bubbles are round. At random loose packing (RLP, “the loosest possible random packing that is mechanically stable”; Onoda and Liniger, 1990), the bubbles deform as they grow. At random close packing (RCP, the maximum random packing), gas propagates in a fracture-like pattern. Therefore, interaction with solids in a crystal-rich upper magma must also affect bubble morphology and rise dynamics during Strombolian eruptions. In this context, we will refer to Taylor bubbles in Newtonian liquids as “slugs” but use the term “bubble” for all geometries of bubbles in non-Newtonian suspensions.

Here, we use analogue experiments to model gas bubbles rising below and into a particle-laden layer, investigating how particles in suspension affect the slug rise model for Strombolian eruptions. We show that particle-rich suspensions affect bubble morphology and bubble rise and generate burst dynamics consistent with observations at Stromboli Volcano, Italy. Our data suggest a weak plug model as a source mechanism for Strombolian eruptions at hydrous open-system mafic volcanoes.

2. Activity at Stromboli Volcano, Italy

Stromboli Volcano is persistently active with eruption recurrence times of 10 – 10^3 seconds (e.g. Barberi et al., 1993; Rosi et al., 2013). Eruptions during “normal activity” last up to tens of seconds and include several pulses with durations of 0.05 - 2 seconds (Patrick et al., 2007; Taddeucci et al., 2013; Gaudin et al., 2014). The frequency and intensity of normal activity at Stromboli varies with time, sometimes within days (Harris and Ripepe, 2007a). Strombolian eruptions are classified into four sub-categories: type 0 emit very few small particles at high velocity; type 1 eject mainly coarse ballistics; type 2 generate ash-rich plumes with (2a) or without (2b) ballistics (Patrick et al., 2007; Harris et al., 2013; Leduc et al., 2015). Eruptions derive from the North-East (NE), central, and South-West (SW) vents, with shorter, louder explosions in the NE (typically type 1), and longer, pulsatory events in the SW (typically type 2; Ripepe and Marchetti, 2002; Chouet et al., 2003; Harris and Ripepe, 2007a).

These eruptions produce pyroclasts with an average of 45 – 55 vol% phenocrysts during normal activity (Landi et al., 2004; Metrich et al., 2010). Plagioclase begins to crystallize at 2 – 4 km depth (Métrich et al., 2010), but plagioclase crystallinity rapidly increases ~800 m below the crater (Landi et al., 2004; Agostini et al., 2013). Crystal-poor basalt resides at depths > 7 km and only erupts during paroxysms (Metrich et al., 2010; LaFelice and Landi, 2011). This volatile-rich lower magma provides the gas source for normal Strombolian eruptions. Therefore, a rheological transition from a crystal-poor basalt to a crystal-rich cap begins at 2 – 4 km depth and accelerates at ~0.8 km depth. These depths correspond to estimated slug source depths of 0.8 and 2.7 km (Burton et al., 2007), estimates which assume, however, that bubbles form at chemical equilibrium and ascend quickly without substantial exchange of volatiles with the melt.

Estimates of gas flux, however, show that Strombolian eruptions account for less than 10% of the total mass of gas erupted; most outgassing occurs via puffing or quiescent degassing (Francis et al., 1993; Allard et al., 1994; Harris and Ripepe, 2007b). Gas compositions indicate that non-explosive outgassing has a shallow source (Burton et al., 2007). Pyroclasts ejected during puffing are less crystalline than in normal explosions (Landi et al., 2011). Puffing generates lower amplitude acoustic signals than Strombolian eruptions, and is generally active in one vent at a time, but migrates between vents, and is therefore interpreted as a train of small weakly overpressured bubbles of shallower origin than those that generate Strombolian eruptions (Ripepe et al., 2007; Landi et al., 2011; Lane et al., 2013).

3. Methods

3.1. Experimental set-up

We performed experiments using the same apparatus as Del Bello et al. (2015) and Capponi et al. (2016), although with a modified bubble injection system (Figure 2), and same low-viscosity liquid as Capponi et al. (2016). A vertical 3-m-high tube of internal diameter D = 0.0257 ± 0.0001 m was connected to a bubble trap at its base and to a vacuum pump at the top to reduce ambient pressure (P_{surf} = 0.3 ± 0.1 kPa, 1 ± 0.2 kPa, 50 ± 1 kPa, and 101 ± 1 kPa) and scale for near-surface gas expansion at Stromboli (James et al., 2008; Lane et al., 2013). The tube was filled to 1.43 ± 0.01 m above the bubble trap with silicone oil (Wacker Chemie AG – AS 100; viscosity 0.1 ± 0.05 Pa s; surface tension 0.021 N/m) and polypropylene particles (A. Schulman – Icorene N4420-1200, sieved by hand). Microscope analysis of 200 particles revealed angular morphologies with an average equivalent sphere diameter of 0.8 mm (standard deviation of 0.48 mm; Supplementary Material). The particle density (900 kg/m^3) was slightly lower than the silicone oil (990 kg/m^3); therefore, the particles rose to the top of the column and, at the start of each experiment, formed a layer of oil + particles (the “cap”) above the pure oil. The caps contained particle masses of 5.4, 14, 23, 46, and 92 grams (± 10 %), which correspond to "packed" cap lengths of approximately 3.5, 8, 13, 25.4, and 53.5 cm respectively (Table 1).

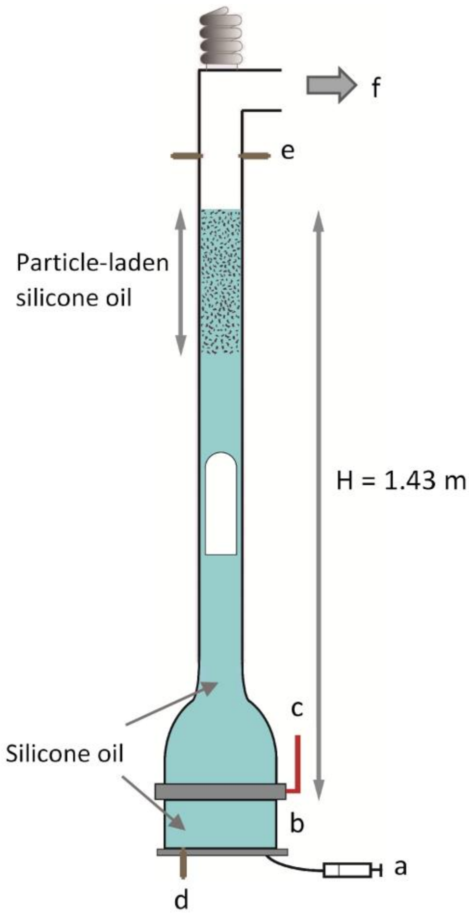

Figure 2: Experimental set-up. Gas slugs were injected through a syringe (a) into a bubble trap (b) and released using a butterfly valve (c). Measurements were made of base liquid pressure (d), gas pressure at the surface (e), along with high speed videos. Pressure at the liquid surface was controlled with a vacuum chamber (f).

To avoid pre-formed pathways within the cap, it was disrupted between each experiment with large gas slugs that generated turbulence. This introduced small bubbles that foamed when ambient pressure was reduced to experiment pressure, and dispersed particles throughout the tube. Particle concentrations were then controlled by allowing the particles to rise until the cap reached the desired length, so that for the same mass of particles, longer caps had lower particle concentrations. For each experiment a bubble of volume 4, 10, 17, 32 or 49 ml (± 10 %) was injected into the bubble trap and prevented from rising by a closed butterfly valve. When released from the trap, the bubble rose as a gas slug in the tube. Cap lengths were non-dimensionalized as a function of internal tube diameter (D). Particle fractions were divided by RCP to generate a normalized particle fraction, φ, for comparison with other work involving particle-rich suspensions. RCP was measured as 47 ± 2 vol% by pouring dry particles in a graduated cylinder (D = 28 mm) and tapping/shaking the container for minutes until the bulk volume was constant. We estimated φ by dividing the calculated cap length at RCP by the measured cap length in each experiment. Particle fractions were overestimated when particle-bearing clusters ejected during experiments remained attached to the tube walls. This error was larger for shorter caps because a small loss of particles caused a larger relative change in cap length. Additionally, as particle contents could vary within the cap, all reported particle fractions were averages of the full cap.

Simply allowing the particles to rise should have created a random *loose* packing because of the small density difference between particles and liquid (Onoda and Liniger, 1990). However, closer packings occurred (φ < 0.92) because residual small bubbles shook the suspension as they ascended through the particle layer during compaction. For our particles, RLP was likely near the median value for packed caps (~40 vol% particles). RCP was not achieved in experiments.

Two differential pressure transducers (Honeywell 163PC01D36; sampling frequency 5 kHz) recorded pressure changes in the air above the liquid surface with respect to the pressure in the vacuum chamber (Lane et al., 2013). Two cameras recorded the experiments: a Basler acA2000-340km filmed the entire column at 300 ± 0.1 fps, and a Canon Powershot G15 recorded only the particle

	Number of exps.	Initial bubble size (mL)	Surface pressure (kPa)	γ (plug-free)	Mass of particles (g)	Cap length (cm)	Dimensionless cap length (D)	Particle content (vol%)	ϕ
	9	4, 10, 17, 32	0.3	8.8 - 70	0	0	0	0	0
	15	4, 10, 17, 32, 49	1	0.83 - 10	0	0	0	0	0
	8	4, 10, 32, 49	1	0.83 - 10	5.4	3 – 10	1.1 – 4.0	11 – 39	0.24 – 0.84
	10	4, 10, 32, 49	50	$(1.4 - 17) \times 10^{-3}$	5.4	3 – 6	1.2 – 2.5	18 – 36	0.39 – 0.77
	4	10, 49	100	$(1.6 - 7.8) \times 10^{-3}$	5.4	3 – 6	1.3 – 2.2	20 – 35	0.43 – 0.75
	8	4, 10, 32, 49	1	0.83 - 10	14	7 – 12	2.8 – 4.8	24 – 42	0.52 – 0.90
	12	4, 10, 32, 49	50	$(1.4 - 17) \times 10^{-3}$	14	8 – 14	3.2 – 5.6	21 – 37	0.45 – 0.79
	8	10, 17, 32, 49	100	$(1.6 - 7.8) \times 10^{-3}$	14	7 – 13	2.8 – 5.1	23 – 42	0.49 – 0.90
	4	10, 32	0.3	22 - 70	22 – 23.5	11 – 13	4.4 – 5.1	38 – 42	0.82 – 0.90
	15	4, 10, 32, 49	1	0.83 - 10	22 – 23.5	12 – 28	4.6 – 11.0	17 – 42	0.37 – 0.90
	10	4, 10, 32, 49	50	$(1.4 - 17) \times 10^{-3}$	23	13 – 20	4.9 – 7.9	24 – 39	0.52 – 0.84
	12	2, 4, 10, 32, 49	100	$(0.32 - 7.8) \times 10^{-3}$	23	12 – 14	4.5 – 5.4	36 – 43	0.76 – 0.92
	4	17	1	3.5	37.2	20 – 53	8.0 – 20.7	15 – 39	0.32 – 0.84
	4	4, 10, 32	0.3	8.8 - 70	46	25	9.6 – 9.9	39 – 40	0.83 – 0.86
	4	4, 10, 32, 49	1	0.83 - 10	46	25 – 27	9.6 – 10.5	37 – 40	0.79 – 0.85
	1	32	0.3	70	92	53	20.7	38	0.8
	2	10, 32	1	2.1 - 6.6	92	52 – 55	20.2 – 21.5	36 – 38	0.77 – 0.81
Total:	130	2 – 49	0.3 – 100	0.00032 - 70	0 – 92	0 – 55	0 – 21.5	0 – 43	0 – 0.92

Table 1: Summary of experimental conditions. A more detailed list is available in Supplementary Material.

layer at 120 ± 1 fps. The images allowed estimates of surface rise velocities, bubble shapes, and whether fragments were ejected during burst. Transducer data and the Basler videos were synchronised through LabVIEW 2014 software.

3.2. Suspension rheology

We measured suspension rheology at 20°C using a HAAKE RheoStress1 with a modified concentric cylinder geometry and gap of 11.7 ± 0.1 mm. We ran the rheometer in controlled stress mode at 10 – 50 Pa with increments of 10 Pa, and for 15 – 50 seconds until the strain rate response to the

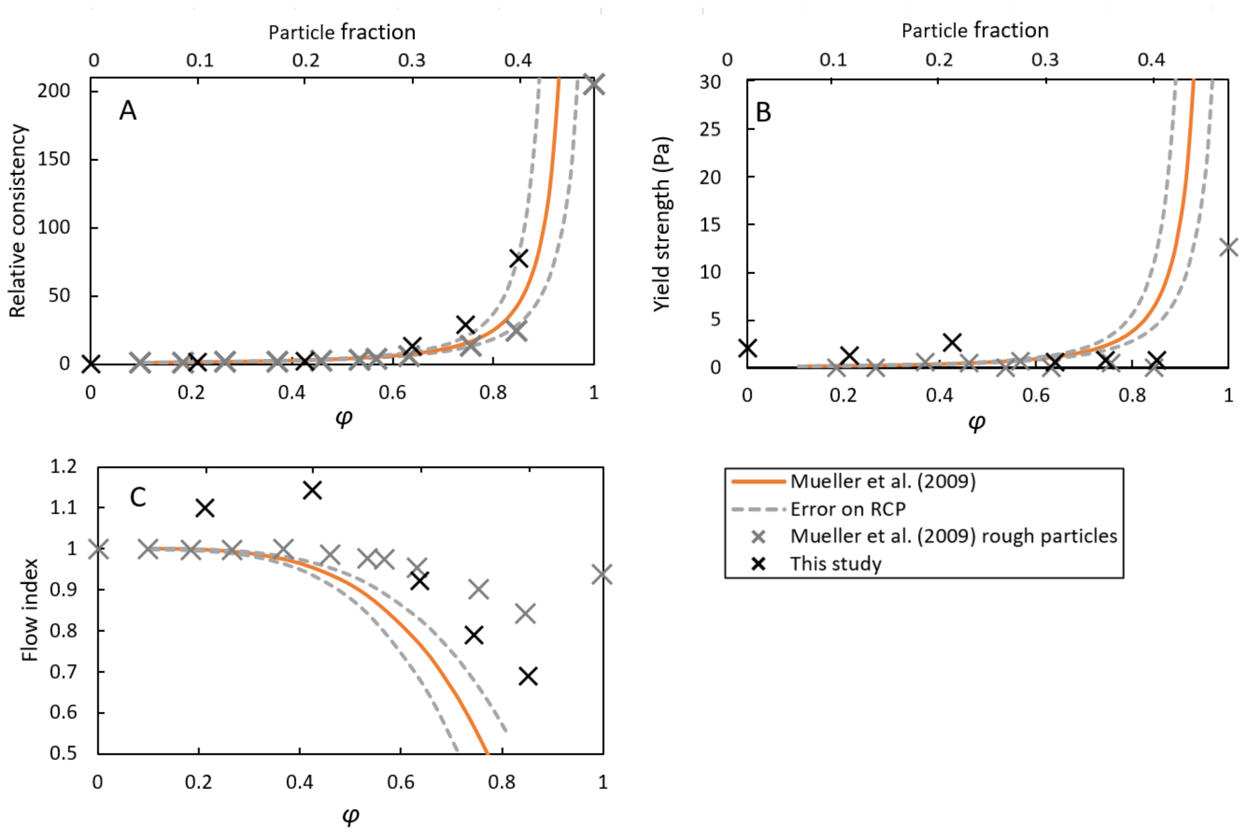

Figure 3: Rheology of the particle-bearing suspensions. Solid lines are calculated from the empirical model by Mueller et al. (2009, 2011), and dashed lines show how the error on RCP (of ± 2) modify the model. Black crosses are rheology measurements with a concentric cylinder (this study), and grey crosses are measurements by Mueller (2009) for crushed particles. Together, these three datasets give an overall idea of cap rheology. A: The relative consistency is the consistency (K) divided by the viscosity of the Newtonian liquid (0.1 Pa s here). K has the dimensions Pa s^n and is equivalent to viscosity when n = 1. B: Yield strength. Experiment yield strengths determined through curve fitting were relatively consistent with the experimental data for crushed particles in Mueller et al. (2009). Our first experimentally measured yield strength occurred at 40 vol% particles (Supplementary Material). C: Flow index indicates whether the suspension is shear-thinning (n <1), shear-thickening (n >1), or Newtonian (n = 1). Here, our data falls between the crushed particles and model in Mueller et al. (2009), possibly indicating large errors. The apparent shear-thickening in experiments with low φ may also have been caused by particle rise.

induced stress equalized; we recorded the strain rate over the last three seconds. Instrumental errors on viscosity are ±0.02 Pa s, although greater errors were caused by bubbles in suspension and particle rise. We fitted our measurements to a Herschel-Bulkley (1926) model:

$$\tau = \tau_y + K\dot{\gamma}^n, \tag{1}$$

where τ is applied stress, τ_y is yield strength, n is flow index, and K is consistency.

Due to the possibility of large experimental errors, we compared our data to models by Mueller et al. (2009, 2011) by determining K_r (relative consistency), τ_y, and n using equations 2.4, 4.1, and 5.2 from Mueller et al. (2009), which requires a fitting parameter, φ_m, that represents the particle fraction at which suspensions can no longer be sheared. We use our measured RCP as a best approximation of φ_m. Indeed, although sheared suspensions typically generate φ_m > RCP, Mueller et al. (2009) generate values close to RCP. The aspect ratio used to determine n was also generated from RCP, using equation 4 in Mueller et al. (2011). Additional details are available in Supplementary Material.

3.3. Scaling considerations

We modelled our experiments assuming that rapid (non-equilibrium) bubble expansion near the surface at the volcano scale can be approximated at laboratory scale by varying surface pressure (P_{surf}; James et al., 2008). James et al. (2009) and Del Bello et al. (2012) define a dimensionless expansion index (γ) for slug flow in a Newtonian liquid as

$$\gamma = \frac{\rho_l g A' V_a}{P_{surf} \pi r^2 (1 - A')}, \tag{2}$$

with ρ_l the liquid density, g the gravitational acceleration, A' the dimensionless cross-sectional area of the falling liquid film (equation (28) in Del Bello et al., 2012), V_a the slug volume at P_{surf} if it were at equilibrium, and r the tube radius. Rapid bubble expansion occurs when γ > 1. Therefore, γ provides an estimate of bubble expansion conditions in the Newtonian liquid below the cap, but ignores the viscous resistance from the cap. Our range of P_{surf} covers the full range of slow (equilibrium) and rapid (non-equilibrium) bubble expansion.

The density and viscosity of the lower liquid allowed bubble rise parameters, such as falling film thickness, to be scaled to bubble rise in the lower (basaltic and crystal-free) magma at Stromboli (Supplementary Table 1; Capponi et al., 2016). To account for uncertainty on cap thickness and crystallinity at Stromboli, we covered a range of thicknesses and particle contents in experiments. We did not attempt to scale particle sizes to crystal sizes at Stromboli. Instead, particle sizes were chosen to avoid wall effects and preserve flow properties. We chose a conservative particle size that fit >30 particles in the inner tube diameter to allow for the counter-flow of liquid + particles during bubble rise in the suspension to approach a 10-particle thickness. Smaller particles could have introduced non-negligible capillary and cohesion forces and increased the particle rise (cap "reset") time between experiments.

Other simplifications included: smooth, cylindrical walls, no density-driven convection, no bubbles in the solids-rich cap, little variation in particle shape/size, a single liquid phase, no diffusion between phases, and an abrupt change from a particle-absent to particle-rich suspension. We therefore ignored the effects of near-surface crystallization, vesiculation, and outgassing on magma convection (Palma et al., 2011; Beckett et al., 2014; Gurioli et al., 2014) and melt viscosity, and did not account for the decrease in overpressure from non-adiabatic bubble expansion (Bagdassarov, 1994). Furthermore, we neglected the effect of crystal-scale bubbles and variations in crystal shape and size on cap rheology. Additional details are available in Supplementary Material.

4. Results

After injection, gas slugs rose through the column of silicone oil until they reached the layer of oil + particles (the cap). Subsequent gas migration behaviors depended on both the particle fraction in the cap and the ratio of bubble size to cap length.

4.1. Slug rise in the particle-free liquid

In a tube filled with a Newtonian liquid, the slug base rises at a constant velocity, while the slug nose accelerates until it bursts at the surface (e.g. Seyfried and Freundt, 2000; James et al., 2008, 2013; Lane et al., 2013; Del Bello et al., 2015). In our experiments, the rise velocity of the slug base in the Newtonian liquid below the particle-bearing cap was constant, regardless of cap parameters and surface pressure. On average, slug base velocity U_s = 0.149 m/s (standard deviation 0.005 m/s). This velocity is within error of the calculated velocity of 0.157 ± 0.009 m/s following Wallis (1969; Supplementary Material).

4.2. Geometrical flow configurations

Slug flow in a liquid overlain by a higher viscosity liquid can be categorized by flow configurations that depend on the relative sizes of the bubble and the cap (Del Bello et al., 2015; Capponi et al., 2016): (1) the bubble is fully encased in the cap at burst, (2) the bubble base is still in the lower liquid at burst, and (3) bubble expansion is such that the lower liquid breaks through the cap (Figure 1). To compare with previous work with Newtonian caps, this section focuses on experiments with surface pressures of 1 kPa because they complement data from Capponi et al. (2016).

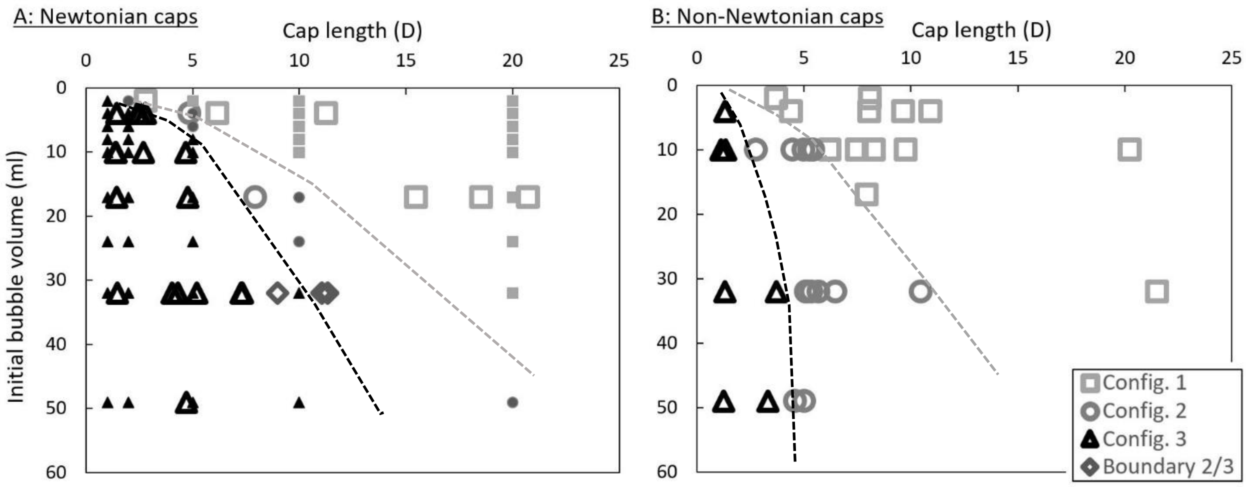

Figure 4: A: Flow configurations in Capponi et al. (2016; smaller filled symbols) and in experiments with Newtonian caps in this study (< ~30 vol% particles; large empty symbols). The “boundary 2/3” category describes experiments that were difficult to categorize due to the opacity of the particle layer: the lower liquid may or may not have reached the surface shortly ahead of the bubble. B: Flow configurations in experiments with non-Newtonian caps (> ~30 vol% particles). Since all experiments with > ~30 vol% particles are shown here, viscosities vary over ~1 order of magnitude. The dashed lines guide the eye to the transitions between regimes. All experiments in this figure have surface pressure = 1 kPa.

Our rheology measurements suggested that caps with < 30 vol% particles behaved as a Newtonian fluid (n ≈ 1; Fig. 3) with effective viscosities between 0.1 Pa s (particle-free) and ~0.8 Pa s (30 vol% particles), which approached those used by Capponi et al. (2016; 1 Pa s). The presence of particles in these experiments did not significantly affect flow configurations (Figure 4A).

At particle contents > 30 vol%, the cap rheology was non-Newtonian (n<1 with a low yield strength, Figure 3). Under these conditions, transitions between configurations occurred at shorter cap lengths (Figure 4B) compared to experiments with particle-poor caps, consistent with the effect of a greater cap viscosity (Capponi et al., 2016). The experiments shown in Figure 4B contained 30 – 43 vol% particles, corresponding to a variation in consistency of slightly over one order of magnitude (Figure 3).

4.3. Rheological flow regimes

Bubble morphology and rise dynamics in the cap depended on cap rheology. Flow regimes were determined through visual characteristics of bubble rise (Figures 5 and 6). In some cases, gradients in particle fraction caused “hybrid” regimes, such that bubbles behaved differently at the bottom and top of the cap.

When the cap comprised a dilute particle suspension, bubble expansion in the lower liquid caused the particle-free oil to intrude into the center of the cap ahead of the bubble (Figure 7A). In the cap, the bubble remained axisymmetric but its diameter decreased and it developed a rounded base. This sequence matches observations of slug flow into a Newtonian liquid of higher viscosity (Del Bello et al., 2015; Capponi et al., 2016), and thus we classify this regime as a ***slug flow regime*** (Figure 5A). At low P_{surf}, the film at the bubble nose broke in several places and discharged a few liquid-particle fragments, in contrast to the particle-free scenario, where bubble burst generated one accelerated droplet.

The ***side flow regime*** occurred with higher particle fractions. Here, bubble expansion in the lower liquid caused a finger of liquid to intrude the side of the cap and, although the lower portion of the cap was diluted by the intruded liquid, most of the cap rose upwards. When it reached the cap, the bubble nose filled the finger and then slowed as it pushed the cap upwards, while the tail of the bubble continued rising as liquid drained from the falling film at the bubble walls. The bubble thus became shorter and wider, and slowly migrated upwards. The duration of coupled rise of the bubble and cap was greater for smaller bubbles and for longer caps with higher particle concentrations. In the cap, the bubble flowed against the tube wall, usually as a linear continuation of the original finger although in some cases it also spiraled slightly (Figure 5B & 7B). The particle suspension remained in one piece, deforming around the bubble. Bubble burst occurred at the side of the tube and was often accompanied by ejection of clasts that fountained above the suspension surface.

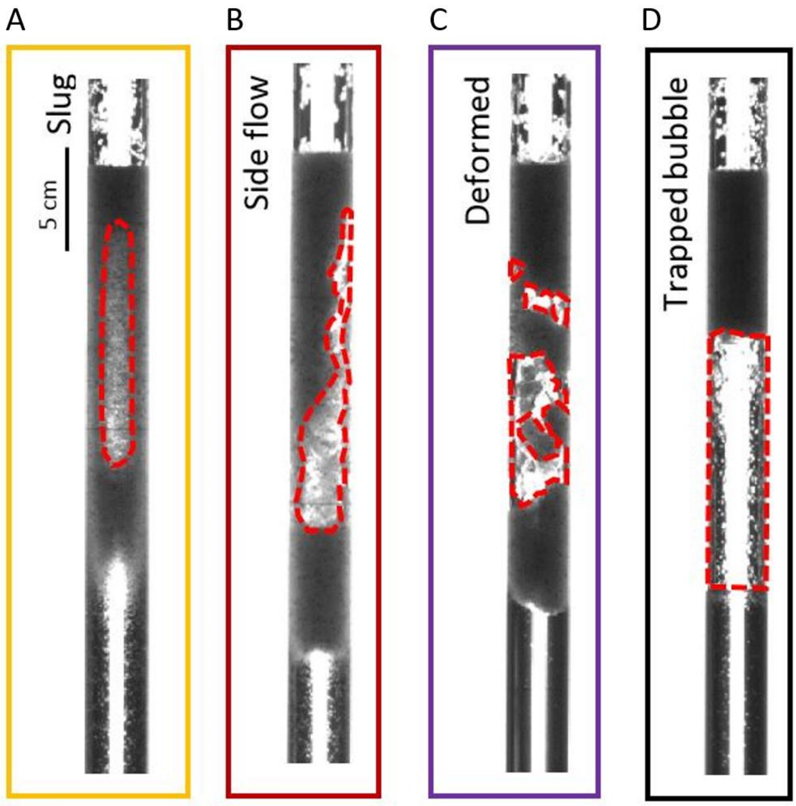

Figure 5: Comparison of the different regimes discussed in this research. These illustrative examples were produced by different experimental conditions.

A further increase in particle fraction induced a transition to the ***deformed regime***. Here, bubble expansion in the lower liquid caused the cap to slide upwards as a plug, presumably with a film of oil at the wall; we did not explore whether the dynamics would be significantly different with a rough wall. Again, the bubble paused before entering the cap; the duration of this pause increased with particle fraction. In the cap, the bubble advanced intermittently, the particle suspension often separated into several pieces, and clusters of liquid + particles slid down the side of the tube as the bubble made its way through the cap (Figure 5C & 7B,C). Accelerations and decelerations of the cap surface reflected variations in bubble expansion rate. The bubble burst at the side of the tube and generated a fountain of small clasts (supplementary video 2).

At high particle fractions and low bubble expansion, some bubbles remained trapped indefinitely below (Figure 5D) or within the cap, thus defining the ***trapped bubble regime***. Bubbles trapped within the cap initially rose in the side flow or deformed regime, then decelerated and stopped. The trapped bubbles could often be mobilized by injecting another slug at the base of the apparatus, when the sudden displacement of the entire column caused by slug injection and expansion was sufficient to push the trapped bubble upwards and break the cap. This process sometimes had to be repeated several times before the trapped gas was mobilized sufficiently to escape.

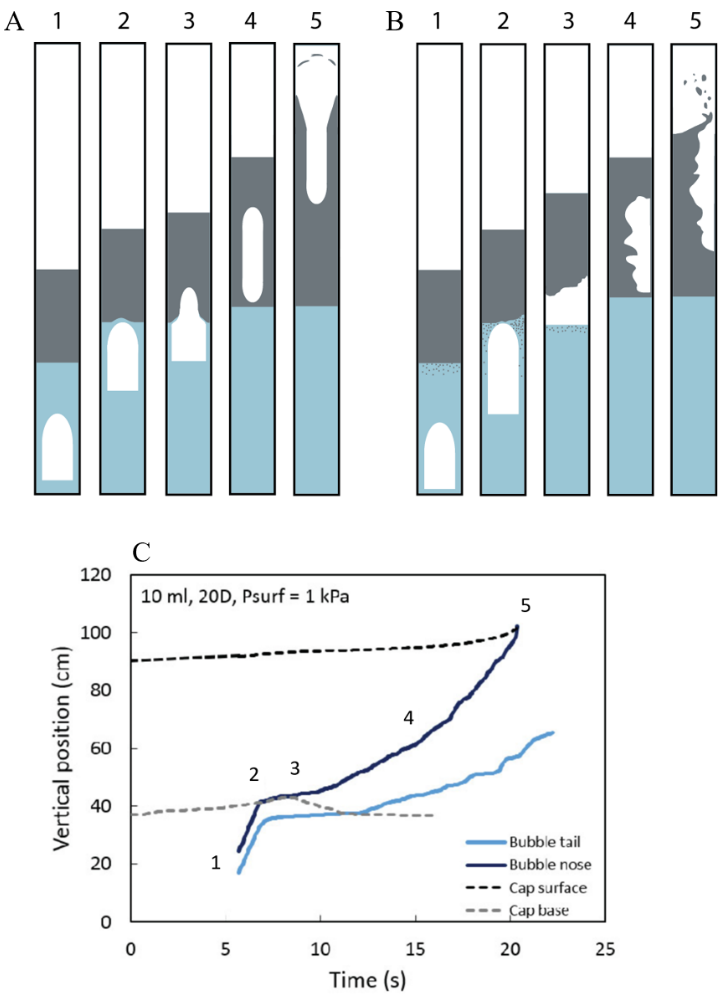

Figure 7: Bubble rise in the rheologically layered experiments can be subdivided into stages of ascent, as shown in (A) for a Newtonian cap and (B) for a non-Newtonian cap. (C) Shows tracks of the bubble, the cap, and the surface of an experiment in the deformed regime, for a bubble of initial volume 10 ml and $\gamma > 1$. First, the slug rose in the lower liquid (1). When the slug reached the cap (2), bubble behavior depended on flow regime. In the slug flow regime, bubbles flowed seamlessly from the lower liquid into the upper liquid. In the side and deformed regimes, bubbles were temporarily trapped below the cap. As the bubble pierced the cap (3), a portion of the liquid + particle suspension flowed down the side of the tube, forming a thick bubble film that is viscously supported by the tube wall. In stage (4), the bubble was fully encased in the cap, and in (5) the bubble burst at the surface. Note that in stage (4) the shear-thinning rheology is visible in the overall curvature of the bubble base position in (C). Base velocities of conduit-filling bubbles are constant in Newtonian liquids (White and Beardmore, 1962; Viana et al., 2003). Here, the bubble base accelerates upward with time as its increasing overpressure interacts with the shear-thinning cap.

4.4. Regime diagrams

Of the four parameters varied in our experiments (particle fraction, initial bubble volume, surface pressure, and cap length), particle fraction provided the dominant control on regime transitions. Bubble expansion, controlled mainly by surface pressure but also by initial bubble size, had a moderate effect. Cap length, while affecting other flow characteristics, did not affect regimes (Figure 6).

Slug flow occurred only at particle fractions <30 vol%, or $\varphi < 0.64$, regardless of other parameters (Figure 6, orange dashed line). The departure from the slug flow regime at $\varphi \approx 0.64$ corresponds approximately to the departure from Newtonian rheology (Figure 3C). Immediately above $\varphi \approx 0.64$, bubbles travelled through the cap in either the side flow or deformed regime. The transition between these regimes depended on both the expansion index γ (an indicator of stress on the cap) and particle fraction. In experiments with $\gamma < 1$ (low bubble expansion), the deformed bubble regime was observed in experiments with particle contents >35 vol% ($\varphi > 0.75$). At $\gamma > 1$, the deformed regime began at ~37 vol% particles ($\varphi \approx 0.80$; Figure 6A).

Bubbles were trapped at $\gamma < 1$ and high particle volume fractions. Notably, all bubbles with $\gamma < 1$ that interacted with a cap containing >37 vol% particles ($\varphi > 0.80$) were trapped, even for thin caps (Figure 6A,B). Bubble entrapment below, rather than within, the cap (Figure 5D) also occurred primarily at $\varphi > 0.80$, although bubble entrapment within the cap occurred at $\varphi > 0.7$, plausibly recording a hybrid regime between trapped bubbles and bubbles that break the surface. All trapped bubbles applied buoyancy forces < 0.6 N on the cap (Figure 6C).

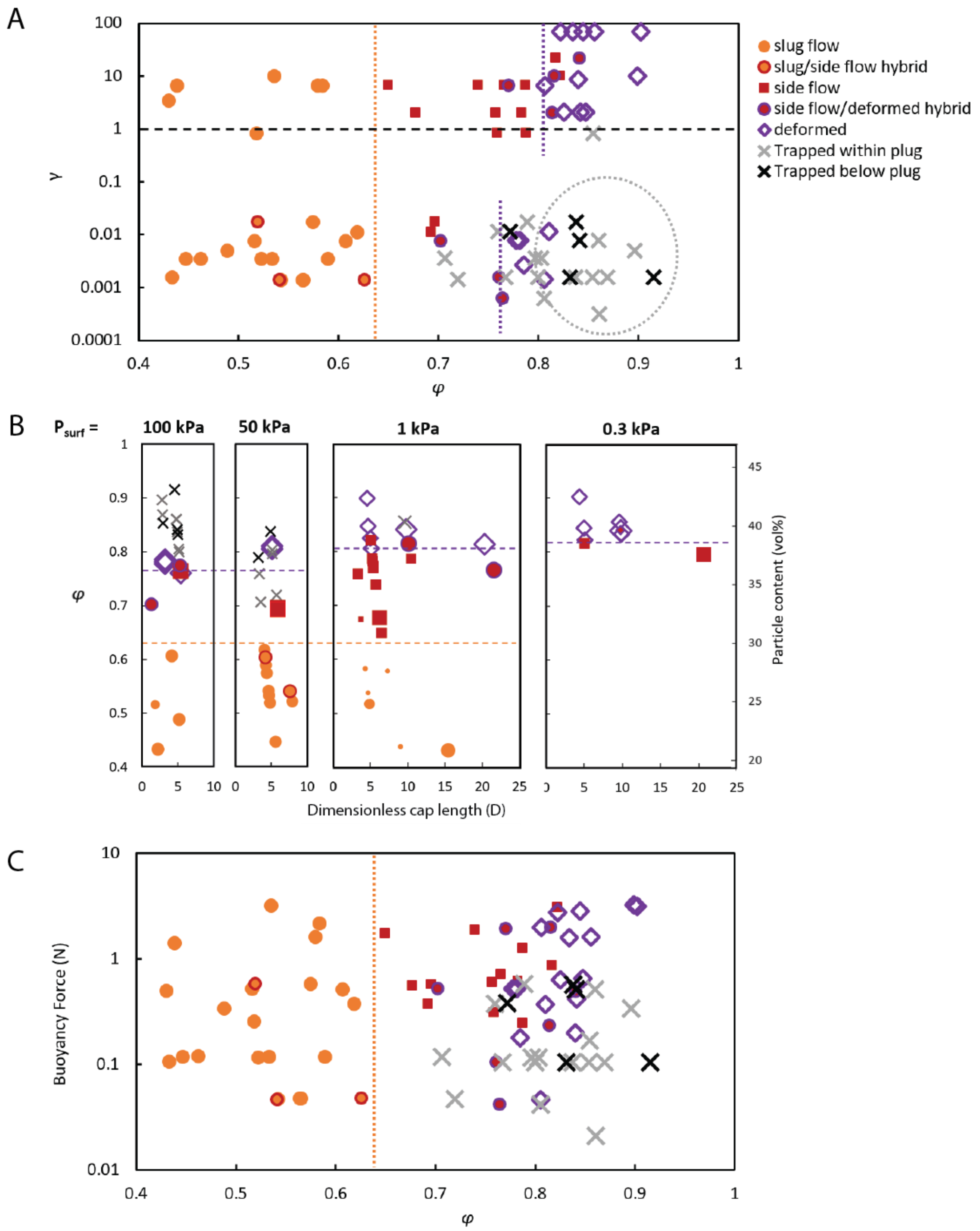

Figure 6: Diagrams of rheological regimes. (A) The dimensionless expansion index γ (James et al., 2009; Del Bello et al., 2012), indicates whether the bubbles could theoretically expand to equilibrium pressure (γ < 1) or not (γ > 1) in the absence of a cap. γ gives an indication of stress on the cap from bubble overpressure and expansion for given initial bubble volumes and surface pressures. Dotted lines represent approximate regime transitions, while the dotted grey circle represents an overall area occupied by the trapped regimes. (B) Deconstruction of the effect of cap length and surface pressure on regime transitions. Each box contains experiments at a different surface pressure. Cap length does not affect regime transitions, but surface pressure does have a minor role. Symbols and dotted lines as in (A), with symbol size indicating configurations: large symbols are configuration 1; medium symbols are configuration 2; smallest are configuration 3 and were only observed at P_{surf} = 1 kPa due to experimental conditions. (C) Bubble buoyancy force applied on the cap when the bubble reaches the bottom of the cap. (Therefore, values depend on both bubble size and cap length.)

4.5. Flow regimes affect surface processes

The particle-rich caps also affected surface level rise, bubble burst dynamics, and acoustic signals emitted during burst. Figure 8 compares maximum surface height variations in experiments containing the same mass of particles (with varying cap lengths) for experiment suites with a given bubble size. An increasing surface height indicates bubble expansion. In the particle-free scenario, rapid bubble expansion accelerated the liquid ahead of the bubble, so that surface height increased substantially. At φ < 0.64 (Newtonian cap), the total surface rise was only slightly reduced, as exemplified by experiments with 17 ml bubbles. Maximum heights in experiments in the side flow and deformed regimes were significantly reduced (by about half) compared to the particle-free scenarios, indicating that the gas was more compressed when it reached the surface.

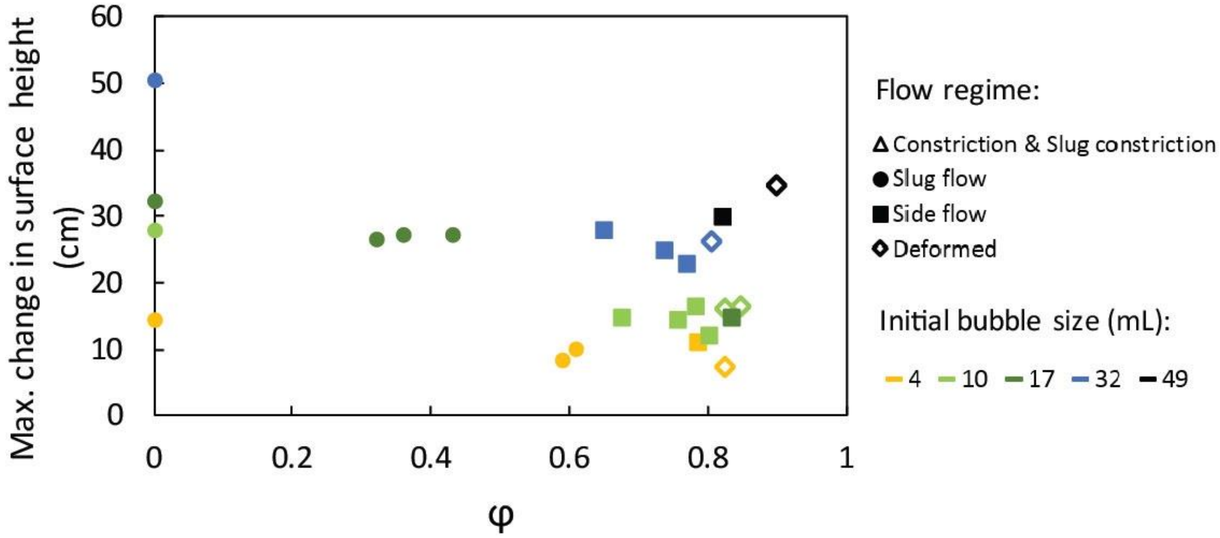

Figure 8: Total surface rise for experiments containing 23 g particles (and 37 g for the 17 mL bubble series) and at P_{surf} = 1 kPa. A surface height of 0 indicates the position at t0, which is 1.43 m above the bubble trap. Since particle mass is constant within each series, an increase in particle fraction causes a decrease in cap length. Colors indicate initial bubble size, and shapes indicate flow regime.

Figure 9 shows examples of acoustic signals for bubble burst in a particle-free (single viscosity) experiment and in two experiments with particle-rich caps. In the side flow and deformed regimes, the acoustic signals were more complex and smaller in amplitude than in the slug flow regime. The decrease in amplitude was complemented by longer signal duration, and thus an increase in the time during which expanding gas was emitted from the ruptured surface. Experiments within the deformed regime that had bigger bubbles and longer caps were more likely to generate several acoustic pulses, further increasing the total signal duration. This pulsatory style was occasionally captured in the camera images as impulsive variations in clast ejection velocities.

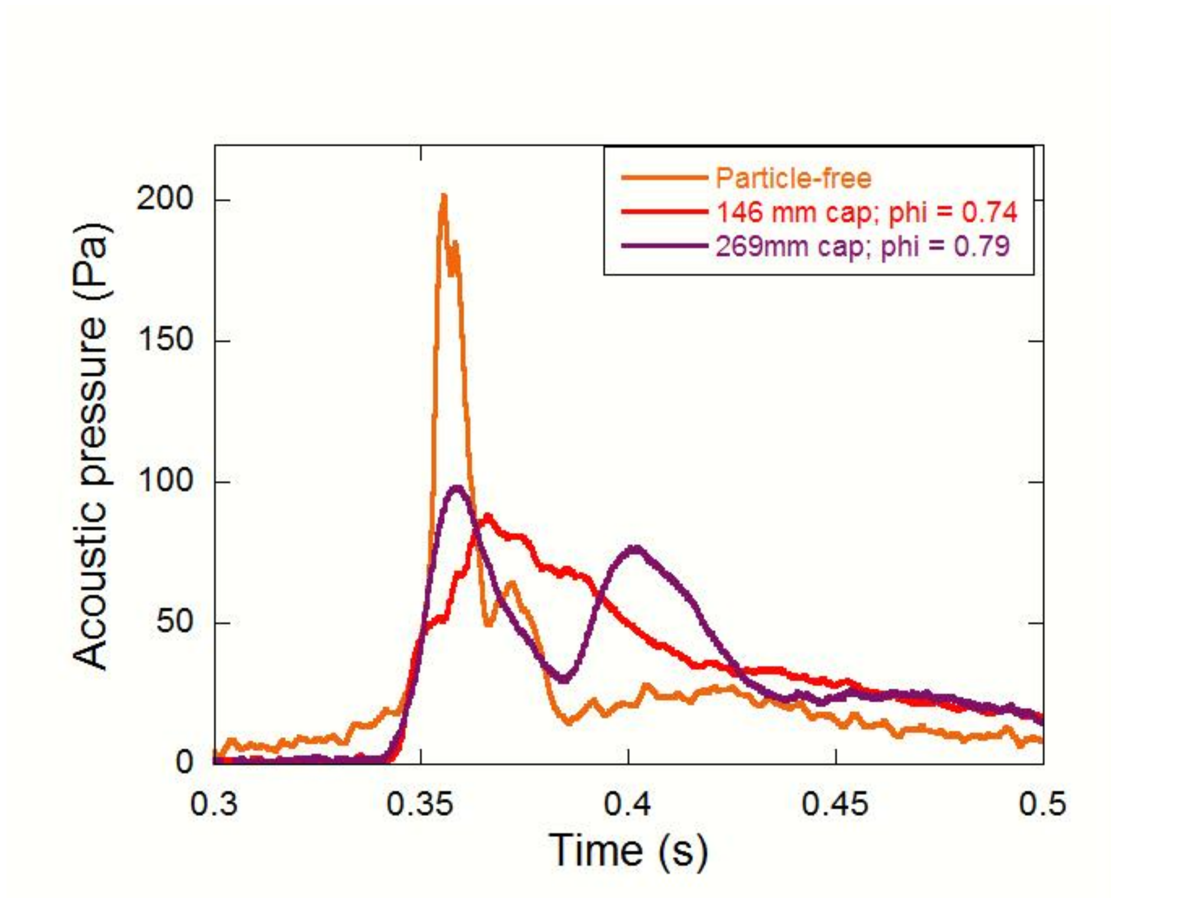

Figure 9: Example acoustic signals for bubbles of initial volume 32 mL, and at surface pressures of 1 kPa. The signal generated by a particle-free experiment (orange) is significantly louder and shorter than the particle-rich examples, which are in the side flow regime (red), and a side/deformed hybrid regime (purple).

5. Discussion

5.1. Flow configurations: comparison with Newtonian experiments

Flow configurations (Fig. 1) are a geometrical consequence of varying bubble and cap sizes; in Newtonian experiments, they control bubble rise beneath the cap, particularly bubble overpressure (Del Bello et al., 2015; Capponi et al., 2017). In our experiments with sufficiently low particle fractions for the cap to be Newtonian (φ < 0.64), flow configurations were not affected by particles (Fig. 4). In fact, the low φ experiments differed from those of Del Bello et al. (2015) and Capponi et al. (2016) only in the style of slug burst in configurations 1 and 2, where the particle-bearing film above the slug nose broke in several places; the result was emission of several particle-liquid clots rather than one accelerated drop. This multi-source rupture was likely caused by particle-generated discontinuities in the rapidly thinning film. For non-Newtonian caps (φ > 0.64), our experiments showed that transitions in flow configurations shifted toward shorter caps, consistent with the effects of increased viscosity (Capponi et al., 2016). These observations suggest that flow configurations can be estimated using simplified rheological descriptions of the cap, regardless of bubble behavior within that cap.

5.2. Rheological flow regimes

Particle fraction in the cap exerted a major control on regime transitions between slug flow, side flow, deformed bubbles, and trapped bubbles, consistent with Oppenheimer et al. (2015). We compare these transitions to the effects of particles on cap rheology (Figure 3).

The first regime transition, from slug flow to side flow, occurred at ~30 vol% particles ($\varphi \approx 0.64$; Fig. 6). At this value, shear-thinning and consistency increased dramatically, indicating the onset of non-Newtonian rheology and weak interactions between particles. The occurrence of particle clusters with a weak yield strength may have contributed to the irregular shape of the bubble as it rose through a heterogeneous cap. Inefficient packing near the tube walls, where particle concentrations and suspension consistency were lower than in the middle of the tube, may have aided bubble rise, while a small yield strength may have suppressed thin falling films, such that a larger physical dimension was required for the exchange down-flow to overcome yield strength.

The next regime transition, from side flow to deformed bubbles, depended weakly upon stress on the cap (generated through bubble expansion, overpressure, and buoyancy; Fig. 6). γ is an imperfect measure of bubble expansion regimes since it ignores the cap, but it approximates stress on the cap from bubble expansion and overpressure. At low stress ($\gamma < 1$), the transition occurred at $\varphi \approx 0.75$. At higher stress ($\gamma > 1$) the transition occurred at $\varphi \approx 0.80$, a value that corresponds with a significant increase in yield strength in particle-bearing suspensions (e.g. Mueller et al., 2009; Brown et al., 2011; Moitra and Gonnermann, 2015). Yield strength is generally associated with pervasive networks of interacting particles (Caricchi et al., 2007; Mueller et al., 2009; Picard et al., 2013).

The transition to deformed bubbles at $\varphi \approx 0.75 - 0.80$ occurs at slightly lower φ than the random loose packing (RLP) for spheres at $\varphi = 0.86$ (Jerkins et al., 2008). RLP is also associated with pervasive particle networks (Onoda and Liniger, 1990) and deformed bubbles (Oppenheimer et al., 2015). Our experiments show an added constraint of applied stress, however, with the regime transition increasing from $\varphi \approx 0.75$ to 0.80 with increased γ. The high bubble overpressure (≤100 kPa) in Oppenheimer et al. (2015) further suggests that RLP may provide the upper bound for transition to deformed bubbles at high stress. Since bubble deformation is controlled primarily by networks of interacting particles, this stress-dependence may suggest that particle networks begin at moderate φ (≈ 0.75) before becoming pervasive at $\varphi \approx 0.86$. However, other factors may affect regime transitions, such as variable particle shape and size, whether the suspension is static or pre-sheared, and experimental uncertainties.

5.3. Bubble trapping mechanism

Bubble rise through the cap requires shearing of the liquid-particle mixture because surface tension prevents bubble rise in the liquid network between particles. As surface tension is negligible on the tube (slug) scale (Bo >> 1), the indefinite trapping of bubbles in or below the cap indicates that buoyancy was insufficient to overcome the strength of the cap in those experiments. Figure 6C shows that buoyancy force and cap rheology (φ) alone do not determine whether a bubble is trapped, and that stresses from bubble overpressure and bubble nose acceleration (reflected in γ; Fig. 6A) are also important. Trapped bubbles occurred exclusively for $\gamma < 1$ and $\varphi > 0.7$ (Fig. 6A); at $\varphi > 0.8$, strong particle networks gave the suspension sufficient strength to arrest all bubbles with $\gamma < 1$. Therefore, bubble trapping may have been enhanced by the smooth experiment walls, which allowed bubble expansion to be accommodated by the cap sliding upwards. However, bubble buoyancy force (< 0.6 N, Fig. 6C) generated a stress on the base of the cap of up to 1200 Pa, which was much greater than the suspension yield strengths (<< 100 Pa based on rotational rheometry; e.g. Mueller et al., 2009, 2011; Tran et al. 2015; Fig. 3), suggesting that bubbles should not have been trapped. The lateral spreading of the bubble may explain this discrepancy. Lateral spreading was driven by deceleration of the bubble nose as it reached the more resistant (and slightly less dense) cap while its base continued to rise in the less viscous pure liquid below. The resulting thinning of the down-flowing annulus of fluid around the bubble reduces the yield stress (relative to the buoyancy stress) required to trap a bubble indefinitely (Dubash and Frigaard, 2004). Furthermore, complete spreading of the bubble to fill the tube below the cap generated horizontal layers; thus gas ascent through the denser cap requires a Rayleigh-Taylor instability of a wavelength limited by the tube diameter (Seropian et al, 2018). Therefore, bubble rise may depend more on the deformation of the cap under its own weight.

Yield strength, consistency, and shear-thinning increase with φ (Figure 3). In some experiments, a vertical increase in particle fraction within the cap caused rising bubbles to decelerate and change regime; we classified these as hybrid regimes. Bubble entrapment *within* the cap occurred over a wide range of average φ (Figure 6), which suggests that either (1) the top of these caps achieved $\varphi > 0.8$ whereupon bubbles became trapped regardless of cap thickness, or (2) the feedback between energy loss during bubble rise and increase in φ was sufficient to trap bubbles even if $\varphi < 0.8$. In this scenario, bubble expansion was insufficient to maintain stress on the cap, such that the apparent viscosity increased and bubbles decelerated until the stress applied by the bubbles fell below the cap's yield strength and/or the bubbles spread laterally to fill the tube. Therefore, the coupled effect of a shear-dependent viscous response and increasing φ near the surface may be an effective mechanism to trap bubbles in the cap.

6. Significance for Stromboli

6.1. Flow regimes in near-surface magma

The near-surface basaltic magma at Stromboli contains 45-55 vol% phenocrysts (Landi et al., 2004; Metrich et al., 2010). Rheological investigations of synthetic basalts observe the onset of yield strength at 20-40 vol% crystals (e.g. Philpotts et al., 1999; Jerram et al., 2003; Picard et al., 2013); experiments on andesites show that bubbles begin to deform and connect at ~20 vol% crystallinity (Lindoo et al., 2017). These values suggest that Strombolian magma is likely within or above the crystallinity range for the deformed bubble regime.

Our experiments in the deformed regime had pulsatory bubble burst events that lasted longer and decayed more slowly than in the slug regime (Figure 9) and produced small clasts that fountained above the surface (supplementary video 2). These characteristics may reflect smaller burst apertures that vibrate as gas is released. With increasing φ, bubble deformation increases (Oppenheimer et al., 2015), hence the bubble aperture is likely to decrease and generate bubble bursts with higher frequency and more gradual gas release (Fig. 9). By comparison, eruptions during normal activity at Stromboli are pulsatory (Taddeucci et al., 2013; Gaudin et al., 2014), last up to tens of seconds (Houghton et al., 2016), have an abrupt start and slow decay (Gaudin et al., 2014), and are accompanied by pyroclast fountains hundreds of meters high. These characteristics are consistent with a highly deformed bubble regime.

6.2. Variability of normal activity

The experimental regime transitions occur over a small range of particle fractions (~17 vol% from the onset of side flow to RCP). Hence small variations in solid fraction may cause significant transitions in gas migration regimes. At Stromboli, the NE vent typically has short, loud and ballistic-generating eruptions (type 1 events) relative to the long, pulsatory, complex ash-generating eruptions from the SW vent (type 2 events; Ripepe and Marchetti, 2002; Harris and Ripepe, 2007a). In our experiments, increasing the particle fraction produced longer burst durations and more complex pulsatory acoustic signals of lower amplitude (Figure 9). This resembles the description for eruptions from the SW vent, consistent with observations that magma in the SW vent is more crystalline (Landi et al., 2011). In contrast, puffing occurs at hotter (lower crystallinity) vents (Landi et al., 2011). We therefore suggest that variations in crystallinity may cause spatial and temporal variations in activity.

6.3. Slug model vs Plug model

There is growing evidence that the slug model for Strombolian eruptions requires modification to account for crystal-rich near-surface magma. Alternative models suggest rupture of a crystal-rich plug as a source mechanism (Gurioli et al., 2014; Suckale et al., 2016). Here bubbles accumulate under the plug until (1) the bubble pressure causes the plug to rupture or (2) the plug becomes gravitationally unstable, and the bubble pressure is suddenly released to the surface.

The near-surface crystal-bearing magma at Stromboli is likely deeper (0.8 km and 2-4 km depth; Landi et al., 2004; Metrich et al., 2010; Agostini et al., 2013) than the onset of rapid (non-equilibrium) bubble expansion ($\gamma > 1$; James et al., 2008; Del Bello et al., 2012), which is estimated to begin at ≤100 m below the crater (Del Bello et al., 2012). In such a case, bubbles reach the cap with $\gamma < 1$, and rapid expansion begins when the bubble is already in the crystal-rich layer. This condition means that bubble rise occurs in a deformed (or other crystal-rich) regime and models predicting overpressure must consider irregular bubble rise in non-Newtonian suspensions. Additionally, if $\gamma < 1$ when the bubble reaches the crystal-rich layer, bubble entrapment may occur either beneath or within that layer. In our experiments with $\gamma < 1$, bubble entrapment is related to yield strength. Since basalts can develop yield strengths at 20 – 40 vol% crystals (e.g. Philpotts et al., 1999; Picard et al., 2013), even moderate crystallinities at depth can trap bubbles. Therefore, breaching the cap may require external modifiers such as tectonic stresses and/or modified rheology and compressibility caused by a reservoir of small bubbles in the cap (Suckale et al., 2016).

The crystal-rich layer can also enable the accumulation and coalescence of smaller bubbles into conduit-sized bubbles that eventually rise through the plug (Belien et al., 2010; Suckale et al., 2016; Barth et al., 2019). Furthermore, trapped bubbles can occur at any level in the crystal-rich magma. Therefore, while the slug model depends on slow slug formation and rapid slug rise such that only one slug can rise in the conduit at any time, a model where bubbles can be trapped or delayed no longer precludes simultaneous rise from depth of several bubbles. Indeed, magma levels in the conduit appear to increase with gas flux (Ripepe et al., 2002), which may indicate increased bubble entrapment.

When analyzed from an equilibrium perspective, gas compositions from normal Strombolian activity suggest source depths of 0.8 and 2.7 km below the craters (Burton et al., 2007). While both source depths may be within crystal-bearing (“high porphyritic”) magma, the shallower source corresponds to the estimated depth of the crystal-rich cap (Landi et al., 2004; Agostini et al., 2013), and is associated with weaker eruptions (Burton et al., 2007). Our data suggest that these bubbles could have been trapped or delayed in a crystal-rich plug. Importantly, bubbles change chemistry by volatile exchange with the surrounding melt. Estimates of bubble source depths (e.g., Burton et al., 2007) assume equilibrium degassing at depth followed by sufficiently fast ascent to preserve the deep gas signature. This leads to erroneous depth estimates if gas chemistry changed without equilibrating during bubble entrapment or hindered ascent (Pichavant et al., 2013).

The likelihood of bubble entrapment in the Stromboli conduit suggests that a weak plug model is reasonable. Importantly, many volcanoes that have Strombolian activity also have moderate-to-high crystallinities. Investigating eruption behavior at other volcanoes alongside crystal textures may help to constrain the role of crystals in Strombolian eruptions. For example, the 2000 eruption at Etna volcano, Italy, alternated between lava fountains (~35 vol% crystals) and Strombolian eruptions (> 55 vol%; Polacci et al., 2006; Giordano et al., 2010), as did activity during the 1943-1952 eruption of Paricutin (with 40-50% crystals; Erlund et al., 2010). At Tungurahua Volcano, Ecuador, which has intermediate magma composition, Strombolian eruptions have lower crystallinity than (and alternate with) Vulcanian eruptions (Wright et al., 2012). Cashman and Sparks (2013) show that Strombolian and Vulcanian eruptions have similar ranges in crystallinity but differ mainly in melt viscosity. These data support the soft plug model for Strombolian eruptions where near-surface magmas have sufficiently high crystallinity to temporarily impede bubble rise, with stronger, more crystalline, less permeable plugs leading to a low-melt-viscosity equivalent of Vulcanian-style plug failure. At the other extreme are Strombolian eruptions formed by rise of individual large bubbles in crystal-poor lava lakes, such as Kilauea and Erebus (e.g. Gerst et al. 2013; Qin et al. 2018).

7. Conclusions

Most models for Strombolian eruptions ignore the effect of crystals on bubble rise. Here, we show that particles modulate the rise of conduit-filling bubbles, generating flow characteristics that depend on particle fraction and stress applied by the bubble on the cap.

If the gas bubbles expand slowly (low stress on the cap), particle-rich suspensions can efficiently trap large bubbles, allowing gas to accumulate below or within the cap before rising through the cap. This is essentially a “weak plug” model. At Stromboli volcano, the crystal-bearing magma is deeper or of similar depth to the onset of rapid (high stress) gas expansion. Therefore, Stromboli may have a weak plug.

During rapid gas expansion in a particle-rich suspension, bubbles are highly deformed, and therefore burst at the surface through a small aperture. Gradual gas release through a vibrating aperture leads to pulsatory fountains of clasts and longer acoustic signals of lower amplitude, which start abruptly and decay slowly. Since burst aperture decreases at higher particle fraction, these features likely become more pronounced as particle fraction increases. These observations fit with observations at Stromboli volcano, suggesting that variations in explosion duration, pulsations, and fountaining may provide insight into near-surface magma crystallinity. This research suggests that Strombolian eruptions are linked to near-surface crystallization, and that local/temporal variations in crystallinity or crystal-bubble interactions may explain variations in degassing style.

8. Acknowledgements

This research was funded by the People Programme (Marie Curie Actions) of the European Union's Seventh Framework Programme (FP7/2007-2013) under the project NEMOH, REA grant agreement number 289976. We would like to thank Einat Lev, Jon Blundy, Bettina Scheu, Marie Edmonds, and Mike Kendall for helpful comments and insights, as well as Heidy Mader and Paul Jarvis for their help with rheology concepts and measurements. We would also like to express our warm appreciation of insightful edits and reviews by Tamsin Mather, Lucia Gurioli, and an anonymous reviewer; unfortunately, due to length constraints we were unable to include all suggested additions.

9. Supplementary videos

Supplementary video 1 shows bubble rise and burst in an experiment in the slug flow regime (φ = 0.36; initial bubble volume = 17 mL). The video is slowed 5x. The start of the video corresponds with bubble injection in the experiment.

Supplementary video 2a shows bubble rise in an experiment in the side flow regime, where bubble burst at the surface was more complex (φ = 0.82; initial bubble volume = 49 mL). The video is slowed 5x and starts at bubble injection. **Supplementary video 2b** shows a close-up of the surface at burst. Video is slowed 10x.

10. Bibliography

1. Agostini, C., A. Fortunati, F. Arzilli, P. Landi, and M. R. Carroll (2013), Kinetics of crystal evolution as a probe to magmatism at Stromboli (Aeolian Archipelago, Italy), *Geochim. Cosmochim. Acta*, 110, 135 – 151, doi:10.1016/j.gca.2013.02.027.
2. Allard, P., Carbonnelle, J., Metrich, N., Loyer, H., and Zettwoog, P. (1994). Sulfur output and magma degassing budget of Stromboli volcano. *Nature*, 368(6469):326–330.

3. Bagdassarov, N. (1994). Pressure and volume changes in magmatic systems due to the vertical displacement of compressible materials. *Journal of Volcanology and Geothermal Research*, 63(1-2):95–100.

4. Barberi, F., Rosi, M., and Sodi, A. (1993). Volcanic hazard assessment at Stromboli based on review of historical data. *Acta Vulcanologica*. 3, 173 – 187.

5. Barth, A., Edmonds, M., and Woods, A. (2019). Valve-like dynamics of gas flow through a packed crystal mush and cyclic strombolian explosions. *Nature Scientific Reports*, 9, 821. DOI: 10.1038/s41598-018-37013-8

6. Beckett, F. M., Burton, M., Mader, H. M., Phillips, J. C., Polacci, M., Rust, A. C., and Witham, F. (2014). Conduit convection driving persistent degassing at basaltic volcanoes. *Journal of Volcanology and Geothermal Research*, 283:19–35.

7. Belien, I. B., Cashman, K. V., and Rempel, A. W. (2010). Gas accumulation in particle-rich suspensions and implications for bubble populations in crystal-rich magma. *Earth and Planetary Science Letters*, 297(1-2):133–140.

8. Blackburn, E. A., Wilson, L., and Sparks, R. S. J. (1976). Mechanisms and dynamics of strombolian activity. *Journal of the Geological Society*, 132(4):429–440.

9. Brown, E., Zhang, H. J., Forman, N. A., Maynor, B. W., Betts, D. E., DeSimone, J. M., and Jaeger, H. M. (2011). Shear thickening and jamming in densely packed suspensions of different particle shapes. *Physical Review E*, 84(3):11.

10. Burton, M., Allard, P., Mure, F., and La Spina, A. (2007). Magmatic gas composition reveals the source depth of slug-driven strombolian explosive activity. *Science*, 317(5835):227–230.

11. Capponi, A., James, M. R., and Lane, S. J. (2016). Gas slug ascent in a stratified magma: Implications of flow organisation and instability for strombolian eruption dynamics. *Earth and Planetary Science Letters*, 435:159–170.

12. Capponi, A., Lane, S., and James, M. (2017). The implications of gas slug ascent in a stratified magma for acoustic and seismic source mechanisms in strombolian eruptions. *Earth and Planetary Science Letters, 468: 101-111, https://doi.org/10.1016/j.epsl.2017.04.008*.

13. Caricchi, L., Burlini, L., Ulmer, P., Gerya, T., Vassalli, M., and Papale, P. (2007). Non-Newtonian rheology of crystal-bearing magmas and implications for magma ascent dynamics. *Earth and Planetary Science Letters*, 264(3-4):402–419.

14. Cashman, K. V. and Sparks, R. S. J. (2013). How volcanoes work: A 25 year perspective. *Geological Society of America Bulletin*, 125(5-6):664–690.

15. Castruccio, A., Rust, A. C., and Sparks, R. S. J. (2010). Rheology and flow of crystal-bearing lavas: Insights from analogue gravity currents. *Earth and Planetary Science Letters*, 297(3-4):471–480.

16. Chouet, B., Dawson, P., Ohminato, T., Martini, M., Saccorotti, G., Giudicepietro, F., De Luca, G., Milana, G., and Scarpa, R. (2003). Source mechanisms of explosions at Stromboli volcano, Italy, determined from moment-tensor inversions of very-long-period data. *Journal of Geophysical Research Solid Earth*, 108(B1).

17. Conte, A. M., C. Perinelli, and R. Trigila (2006), Cooling kinetics experiments on different Stromboli lavas: Effects on crystal morphologies and phases composition, *J. Volcanol. Geotherm. Res.*, 155(3 – 4), 179 – 200, doi:10.1016/j.jvolgeores.2006.03.025.

18. Del Bello, E., Lane, S. J., James, M. R., Llewellin, E. W., Taddeucci, J., Scarlato, P., and Capponi, A. (2015). Viscous plugging can enhance and modulate explosivity of strombolian eruptions. *Earth and Planetary Science Letters*, 423:210–218.

19. Del Bello, E., Llewellin, E. W., Taddeucci, J., Scarlato, P., and Lane, S. J. (2012). An analytical model for gas overpressure in slug-driven explosions: Insights into strombolian volcanic eruptions. *Journal of Geophysical Research-Solid Earth*, 117.

20. Edwards, M. J., Pioli, L., Andronico, D., Scollo, S., Ferrari, F., Cristaldi, A. (2018) Shallow controlling factors on the explosivity of basaltic magmas: The May 17–25 eruption of Etna volcano (Italy). *JVGR*, doi:10.1016/j.jvolgeores.2018.05.015

21. Erlund, E.J., Cashman K.V., Wallace, P.J., Pioli, L., Rosi, M., Johnson E., Delgado Granados H. (2010). Compositional evolution of magma from Parícutin Volcano, Mexico: The tephra record. *Journal of Volcanology and Geothermal Research*, 167-187. DOI: 10.1016/j.jvolgeores.2009.09.015

22. Francis, P., Oppenheimer, C., and Stevenson, D. (1993). Endogenous growth of persistently active volcanoes. *Nature*, 366(6455):554–557.

23. Gaudin, D., Taddeucci, J., Scarlato, P., Moroni, M., Freda, C., Gaeta, M., and Palladino, D. M. (2014). Pyroclast tracking velocimetry illuminates bomb ejection and explosion dynamics at Stromboli (Italy) and Yasur (Vanuatu) volcanoes. *Journal of Geophysical Research-Solid Earth*, 119(7):5384–5397.

24. Gaudin, D., J. Taddeucci, P. Scarlato, E. del Bello, T. Ricci, T. Orr, B. Houghton, A. Harris, S. Rao, and A. Bucci (2017). Integrating puf fi ng and explosions in a general scheme for Strombolian-style activity, J. Geophys. Res. Solid Earth, 122, 1860 – 1875, doi:10.1002/2016JB013707.

25. Gerst, A., M. Hort, R. C. Aster, J. B. Johnson, and P. R. Kyle (2013), The first second of volcanic eruptions from the Erebus volcano lava lake, Antarctica—Energies, pressures, seismology, and infrasound, J. Geophys. Res. Solid Earth, 118, 3318–3340, doi:10.1002/jgrb.50234

26. Giordano, D., Polacci, M., Papale P., and Caricchi, L. (2010). Rheological control on the dynamics of explosive activity in the 2000 summit eruption of Mt. Etna, *Solid Earth*, 1: 61-69.

27. Gurioli, L., Colo, L., Bollasina, A. J., Harris, A. J. L., Whittington, A., and Ripepe, M. (2014). Dynamics of strombolian explosions: Inferences from field and laboratory studies of erupted bombs from Stromboli volcano. *Journal of Geophysical Research-Solid Earth*, 119(1):319–345.

28. Harris, A. and Ripepe, M. (2007a). Synergy of multiple geophysical approaches to unravel explosive eruption conduit and source dynamics - a case study from Stromboli. *Chemie Der Erde-Geochemistry*, 67(1):1–35.

29. Harris, A., and M. Ripepe (2007b), Temperature and dynamics of degassing at Stromboli, *J. Geophys. Res.*, 112, B03205, doi:10.1029/2006JB004393

30. Harris, A. J. L., Delle Donne, D., Dehn, J., Ripepe, M., and Worden, A. K. (2013). Volcanic plume and bomb field masses from thermal infrared camera imagery. *Earth and Planetary Science Letters*, 365:77–85.

31. Hasan, A. H., Mohammed, S. K., Pioli, L., Hewakandamby, B. H., Azzopardi, B. J. (2019). Gas rising through a large diameter column of very viscous liquid: Flow patterns and their dynamics characteristics. *International Journal of Multiphase Flow*. 116, 1 – 14.

32. Herschel, W. H. and Bulkley, R. (1926). Konsistenzmessungen von gummi-benzoll¨osungen. *Kolloid-Zeitschrift*, 39(4):291–300.

33. Hoover, S. R., Cashman, K. V., and Manga, M. (2001). The yield strength of subliquidus basalts - experimental results. *Journal of Volcanology and Geothermal Research*, 107(1-3):1–18.

34. Houghton, B. F., Taddeucci, J., Andronico, D., Gonnermann, H. M., Pistolesi, M., Patrick, M. R., Orr, T. R., Swanson, D. A., Edmonds, M., Gaudin, D., Carey, R. J., and Scarlato, P. (2016). Stronger or longer: Discriminating between hawaiian and strombolian eruption styles. *Geology*, 44(2):163–166.

35. James, M. R., Lane, S. J., and Chouet, B. A. (2006). Gas slug ascent through changes in conduit diameter: Laboratory insights into a volcano-seismic source process in low-viscosity magmas. *Journal of Geophysical Research-Solid Earth*, 111(B5).

36. James, M. R., Lane, S. J., and Corder, S. B. (2008). Modelling the rapid near-surface expansion of gas slugs in low-viscosity magmas. *Geological Society*, London, Special Publications, 307(1):147–167.

37. James M.R., Lane S.J., Wilson L., and Corder S.B. (2009). Degassing at low magma-viscosity volcanoes: Quantifying the transition between passive bubble-burst and Strombolian eruption. *Journal of Volcanology and Geothermal Research*, 180. 81 – 88.

38. James, M. R., Lane, S. J., and Houghton, B. F. (2013). Unsteady explosive activity. In Fagents, S. A., Gregg, T. K. P., and Lopes, R. M. C., editors, *Modeling Volcanic Processes*, pages 107–128. Cambridge University Press.

39. Jerkins, M., Schroter, M., Swinney, H. L., Senden, T. J., Saadatfar, M., and Aste, T. (2008). Onset of mechanical stability in random packings of frictional spheres. *Physical Review Letters*, 101(1).

40. Jerram, D. A., Cheadle, M. J., and Philpotts, A. R. (2003). Quantifying the building blocks of igneous rocks: Are clustered crystal frameworks the foundation? *Journal of Petrology*, 44(11):2033–2051.

41. La Felice, S., and Landi, P. (2011). A spatter-forming, large-scale paroxysm at Stromboli Volcano (Aeolian Islands, Italy): insight into magma evolution and eruption dynamics. *Bulletin of Volcanology*, 73(9), 1393–1406. Doi: 10.1007/s00445-011-0476-x

42. Landi, P., Marchetti, E., La Felice, S., Ripepe, M., and Rosi, M. (2011). Integrated petrochemical and geophysical data reveals thermal distribution of the feeding conduits at Stromboli volcano, italy. *Geophysical Research Letters*, 38.

43. Landi, P., Metrich, N., Bertagnini, A., and Rosi, M. (2004). Dynamics of magma mixing and degassing recorded in plagioclase at Stromboli (aeolian archipelago, Italy). *Contributions to Mineralogy and Petrology*, 147(2):213–227.

44. Lane, S. J., James, M. R., and Corder, S. B. (2013). Volcano infrasonic signals and magma degassing: First-order experimental insights and application to Stromboli. *Earth and Planetary Science Letters*, 377:169–179.

45. Lautze, N. C., Houghton, B. F. (2005). Physical mingling of magma and complex eruption dynamics in the shallow conduit at Stromboli volcano, Italy. *Geology*, 33(5), 425-428. Doi: 10.1130/G21325.1

46. Leduc, L., Gurioli, L., Harris, A., Colo, L., and Rose-Koga, E. F. (2015). Types and mechanisms of strombolian explosions: characterization of a gas-dominated explosion at Stromboli. *Bulletin of Volcanology*, 77(1).

47. Lindoo A., Larsen J. F., Cashman K. V., Oppenheimer J. (2017) Crystal controls on permeability development and degassing in basaltic andesite magma. *Geology*, 45 (9), 831 – 834.

48. Mader, H. M., Llewellin, E. W., and Mueller, S. P. (2013). The rheology of two-phase magmas: A review and analysis. *Journal of Volcanology and Geothermal Research*, 257:135–158.

49. Metrich, N., Allard, P., Aiuppa, A., Bani P., Bertagnini A., Shinohara H., Parello F., Di Muro A., Garaebiti E., Belhadj O., Massare D (2011). Magma and Volatile Supply to Post-collapse Volcanism and Block Resurgence in Siwi Caldera (Tanna Island, Vanuatu Arc). Journal of petrology 52(6), 1077-1105.

50. Metrich, N., Bertagnini, A., and Di Muro, A. (2010). Conditions of magma storage, degassing and ascent at Stromboli: New insights into the volcano plumbing system with inferences on the eruptive dynamics. *Journal of Petrology*, 51(3):603–626.

51. Moitra, P. and Gonnermann, H. M. (2015). Effects of crystal shape- and size-modality on magma rheology. *Geochemistry Geophysics Geosystems*, 16(1):1–26.

52. Mueller, S., Llewellin, E. W., and Mader, H. M. (2009). The rheology of suspensions of solid particles. *Proceedings of the Royal Society a-Mathematical Physical and Engineering Sciences*, 466(2116):1201–1228.

53. Mueller, S., Llewellin, E. W., and Mader, H. M. (2011). The effect of particle shape on suspension viscosity and implications for magmatic flows. *Geophysical Research Letters*, 38:5.

54. Onoda, G. Y. and Liniger, E. G. (1990). Random loose packings of uniform spheres and the dilatancy onset. *Physical Review Letters*, 64(22):2727–2730.

55. Oppenheimer, J., Rust, A., Cashman, K., and Sandnes, B. (2015). Gas migration regimes and outgassing in particle-rich suspensions. *Frontiers in Physics*, 3:60.

56. Palma, J. L., Blake, S., and Calder, E. S. (2011). Constraints on the rates of degassing and convection in basaltic open-vent volcanoes. *Geochemistry Geophysics Geosystems*, 12.

57. Patrick, M. R., Harris, A. J. L., Ripepe, M., Dehn, J., Rothery, D. A., and Calvari, S. (2007). Strombolian explosive styles and source conditions: insights from thermal (FLIR) video. *Bulletin of Volcanology*, 69(7):769–784.

Parfitt, E. A. (2004) A discussion of the mechanisms of explosive basaltic eruptions. Journal of Volcanology and Geothermal Research, 134 (102), 77-107.

58. Philpotts, A. R., Brustman, C. M., Shi, J. Y., Carlson, W. D., and Denison, C. (1999). Plagioclase-chain networks in slowly cooled basaltic magma. *American Mineralogist*, 84(11-12):1819–1829.

59. Picard, D., Arbaret, L., Pichavant, M., Champallier, R., and Launeau, P. (2013). The rheological transition in plagioclase-bearing magmas. *Journal of Geophysical Research-Solid Earth*, 118(4):1363–1377.

60. Pichavant, M., Di Carlo, I., Rotolo, S. G., Scaillet, B., Burgisser, A., Le Gall, N., and Martel, C. (2013). Generation of co2-rich melts during basalt magma ascent and degassing. *Contributions to Mineralogy and Petrology*, 166(2):545–561.

61. Polacci, M., Corsaro, R. A., and Andronico, D. (2006) Coupled textural and compositional characterization of basaltic scoria: Insights into the transition from Strombolian to fire fountain activity at Mount Etna, Italy. *Geology*. 34 (3): 201-204. doi: 10.1130/G22318.1

62. Qin, Z., Soldati, A., Santana, L. C. V., Rust, A. C., Suckale, J., & Cashman, K. V. (2018). Slug stability in flaring geometries and ramifications for lava-lake degassing. Journal of Geophysical Research: Solid Earth.doi:10.1029/2018jb016113

63. Ripepe, M. and Marchetti, E. (2002). Array tracking of infrasonic sources at Stromboli volcano. *Geophysical Research Letters*, 29(22).

64. Ripepe, M., Harris A. J. L., Carniel R. (2002). Thermal, seismic and infrasonic evidences of variable degassing rates at Stromboli volcano. *Journal of Volcanology and Geothermal Research*, 118, 285-297.

65. Ripepe, M., Marchetti, E., and Ulivieri, G. (2007). Infrasonic monitoring at stromboli volcano during the 2003 effusive eruption: Insights on the explosive and degassing process of an open conduit system. *Journal of Geophysical Research-Solid Earth*, 112(B9).

66. Rosi, M., Pistolesi, M., Bertagnini, A., Landi, P., Pompilio, M., & Di Roberto, A. (2013). Chapter 14 Stromboli volcano, Aeolian Islands (Italy): present eruptive activity and hazards. *Geological Society*, London, Memoirs, 37(1), 473–490. doi:10.1144/m37.14

67. Seyfried, R., and Freundt, A., 2000, Experiments on conduit flow and eruption behaviour of basaltic volcanic eruptions. J. Geophys. Res., v. 105, no. B10, p. 727-740, doi:10.1029/2000JB900096

68. Suckale, J., Keller T., Cashman K. V., and Persson P.-O. (2016) Flow-to-fracture transition in a volcanic mush plug may govern normal eruptions at Stromboli, *Geophys. Res. Lett.*, 43, 12071 – 12081. doi:10.1002/2016GL071501.

69. Taddeucci, J., Palladino, D. M., Sottili, G., Bernini, D., Andronico, D., and Cristaldi, A. (2013). Linked frequency and intensity of persistent volcanic activity at Stromboli (Italy). *Geophysical Research Letters*, 40(13):3384–3388.

70. Tran, A., Rudolph, M. L., and Manga, M. (2015). Bubble mobility in mud and magmatic volcanoes. *Journal of Volcanology and Geothermal Research*, 294:11–24.

71. Vergniolle, S. (1998). Modeling two-phase flow in a volcano. *13th Australasian Fluid Mechanics Conference.*

72. Viana, F., Pardo, R., Yanez, R., Trallero, J. L., and Joseph, D. D. (2003). Universal correlation for the rise velocity of long gas bubbles in round pipes. *Journal of Fluid Mechanics*, 494:379–398.

73. von der Lieth, J. and Hort, M. (2016). Slug ascent and associated stresses during strombolian activity with non-Newtonian rheology. *Journal of Geophysical Research: Solid Earth*, 121(7):4923–4942.

74. White, E.T. and Beardmore R.H. (1962). The velocity of rise of single cylindrical air bubbles through liquids contained in vertical tubes. *Chem. Eng. Sci.* 17, 351-361.

75. Wright, H. M. N., Cashman, K. V., Mothes, P. A., Hall, M. L., Ruiz, A. G., and Le Pennec, J. L. (2012). Estimating rates of decompression from textures of erupted ash particles produced by 1999-2006 eruptions of Tungurahua volcano, Ecuador. *Geology*, 40(7):619–622.